

Ag on a Ni vicinal surface: Coupling Stranski-Krastanov and “magic” heteroepitaxial growthAmandine Bellec,^{1,2,*} Yves Garreau,^{1,2} Jérôme Creuze,³ Alina Vlad,¹ Frederic Picca,¹
Michèle Sauvage-Simkin,¹ and Alessandro Coati¹¹SOLEIL Synchrotron, L'Orme des Merisiers, Saint-Aubin BP 48, 91190 Gif-sur-Yvette, France²Laboratoire Matériaux et Phénomènes Quantiques, Université Paris Diderot, Sorbonne Paris Cité, CNRS, UMR 7162, 75013 Paris, France³ICMMO/SP2M, UMR8182, Université Paris Sud, 15 rue Georges Clémenceau, 91405 Orsay cedex, France

(Received 7 April 2017; revised manuscript received 13 June 2017; published 9 August 2017)

Using vicinal surfaces as a template for heteroepitaxial growth offers a unique possibility to control the orientation and the crystallinity of the grown layer. The study presented here focuses on the growth of Ag on a carefully chosen Ni(11 9 9) substrate. Ag adopts a Stranski-Krastanov growth mode with a slightly constrained wetting layer limited to two monolayers on which well crystallized islands grow. The specific orientation of the Ni substrate leads to Ag(7 9 9) orientation for the Ag thin film and it prevents the formation of twin and stacking fault.

DOI: [10.1103/PhysRevB.96.085414](https://doi.org/10.1103/PhysRevB.96.085414)**I. INTRODUCTION**

Metal-on-metal growth has been studied for a long time on a large variety of metals (homoepitaxy) and metal couples (heteroepitaxy), at least for substrates with low Miller index orientations [1,2]. The work on homoepitaxy has conducted to the possibility to predict the metallic growth modes [3]. For Ag, it has been demonstrated theoretically and experimentally that three-dimensional growth is obtained [4,5]. One needs to use specific growth conditions [4] or surfactant [6,7] to induce a layer-by-layer growth. Using a substrate of another nature is another way to modify the growth mode and induce new properties. Nevertheless, Stranski-Krastanov growth mode is usually observed for Ag on various surfaces such as W(110) [8,9] or Ni(111) [10,11]. The case of the Ag/Ni system is particularly interesting since Ag and Ni are immiscible in bulk, thus leading to a sharp interface. This induces, for example, the strong localization of quantum well states [10].

In this context, vicinal substrates can serve as templates to obtain a better control of the growth process. However, vicinal surfaces are not always stable and can undergo spontaneous faceting [12,13]. Bartolini *et al.* [14] interpreted the stability of the obtained morphology by introducing the concept of “magic” orientations of the facets which appear when the terraces contain an integer number of reconstruction cells. Vicinal surface faceting can also be induced by a submonolayer deposit in the very initial stage of heteroepitaxy [15–17]. For example, for submonolayer Ag deposits on a Cu vicinal surface a periodic faceting with a regular succession of bare Cu- and Ag-covered stripes was observed [18,19]. The driving force for this organization is the existence of a perfect match between step periods (Λ) of the substrate and of the deposited material surface on the covered facet. For a given couple of metals, this can only be fulfilled for specific orientations corresponding to the “magic” heteroepitaxy conditions introduced in Ref. [20] as schematized in Fig. 1, in which the step period of the grown layer coincides with the vicinal substrate one. Table I

summarizes some of the vicinal orientations with (1 1 1) terraces and the corresponding step periods for Ni, Cu, and Ag elements. After screening a large number of vicinal surfaces of different metals one could identify specific couples with a very good matching of the step period Λ . One can see the matching between the step periods of the Cu(2 1 1) and the Ag(1 3 3) surfaces, which is the driving force for the observed magic heteroepitaxial growth [20]. The couple Ni(11 9 9) and Ag(7 9 9) constitutes an optimal candidate, as the step periods Λ are $\Lambda_{\text{Ni}(1199)} = 2.096$ nm and $\Lambda_{\text{Ag}(799)} = 2.095$ nm, respectively. In addition to the substrate nature, the main difference between the Ni(11 9 9) and the Cu(2 1 1) surfaces is the magnitude of the step period. Indeed, the Ni(11 9 9) surface presents a step period three times larger than $\Lambda_{\text{Cu}(211)}$ (Table I). One of the underlying questions is then to know if the magic heteroepitaxial growth can be generalized for large step periods and for other couples of materials. If so, the deposition of Ag should lead to the formation of a homogeneous layer presenting a (7 9 9) orientation (Table I). In addition, the chosen substrate Ni(11 9 9) presents terraces containing $9 + 2/3$ closed pack Ni atom rows with {100} microfacets at the step edges, whereas Ag(7 9 9) presents terraces containing $8 + 1/3$ closed pack Ag atom rows with {111} microfacets at the step edges. Thus, one can expect a reverse fcc stacking sequence in the epilayer. A similar phenomenon is observed in the case of Co growth on Au vicinal surfaces [21], in which the Co film can be “forced” to adopt a fcc structure in spite of the hcp packing observed in case of growth on nominal substrates.

We thus studied the growth of Ag on a Ni(11 9 9) vicinal substrate used as a template. The combination of grazing-incidence x-ray diffraction (GIXD) and scanning tunneling microscopy (STM) measurements together with molecular statics (MS) simulations enables us to demonstrate the formation of a homogenous 2-monolayer-thick wetting layer of Ag with a (7 9 9) orientation on the Ni(11 9 9) surface. As on Ni(1 1 1), here also Ag grows in a Stranski-Krastanov mode. However, thanks to the vicinal substrate, the extra deposition of Ag leads to the growth of well crystallized islands, which are perfectly oriented with respect to the wetting layer.

*Corresponding author: amandine.bellec@univ-paris-diderot.fr

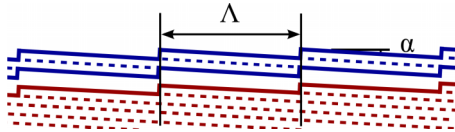


FIG. 1. “Magic” epitaxial growth. Λ is the step periodicity and α is the miscut angle with respect to the $[1\ 1\ 1]$ direction.

II. EXPERIMENTAL AND SIMULATION DETAILS

A. X-ray diffraction and scanning tunneling microscopy

All the experiments were carried out in ultrahigh vacuum (UHV, base pressure of 10^{-10} mbar). Prior to any Ag deposition, the Ni(11 9 9) substrate was cleaned by repeated cycles of Ar^+ sputtering (1 keV) and annealing (700°C). The deposition of Ag was done by electron-beam evaporation from a Mo crucible. The Ag deposition was calibrated afterward by Rutherford backscattering with a 10% error. Several samples with Ag coverages in the range of 2.5–6 monolayers (MLs) were prepared. The samples were annealed after the Ag deposition.

All the measurements were carried out on the Surfaces and Interfaces X-ray Scattering (SixS) beamline at synchrotron SOLEIL. The UHV end station comprises four interconnected chambers dedicated respectively to sample preparation, STM measurements (equipped with an STM 150 Aarhus, Specs), sample storage, and the GIXD measurements [(4+3)-circle diffractometer, Newport-Micro controle]. All the GIXD measurements were performed at an energy of 18.4 keV and an incident angle of $\mu = 0.15^\circ$.

For the GIXD measurements, a so-called (11 9 9) orthogonal basis was used. All indexes and vectors are given with respect to the fcc lattice. The $\vec{a}_{(1199)} = \frac{1}{2}[\bar{1}8\ 11\ 11]$ and $\vec{b}_{(1199)} = \frac{1}{2}[0\ \bar{1}\ 1]$ vectors are perpendicular and parallel to the step edges respectively as schematized in Fig. 2. The $\vec{c}_{(1199)} = [11\ 9\ 9]$ is normal to the average Ni surface. All the GIXD measurements are presented with $(hkl)_{(1199)}$ corresponding to the (11 9 9) basis. These $(hkl)_{(1199)}$ indexes can be transformed into the Miller indexes of the Ni fcc lattice by the following matrix:

$$\begin{pmatrix} h \\ k \\ l \end{pmatrix}_{\text{fcc}} = \frac{1}{283} \begin{pmatrix} -18 & 0 & 11 \\ 11 & -283 & 9 \\ 11 & 283 & 9 \end{pmatrix} \begin{pmatrix} h \\ k \\ l \end{pmatrix}_{(1199)}. \quad (1)$$

TABLE I. Step periods (Λ) for different (1 1 1) vicinal surfaces for Ni, Cu, and Ag elements with an average $(hkl)_{\text{fcc}}$ orientation. n is the number of atomic rows per terraces and α is the angle between the $[hkl]_{\text{fcc}}$ and the $[1\ 1\ 1]$ directions. The $(p-2, p, p)$ surfaces are exhibiting $\{111\}$ microfacets, while the $(p+1, p-1, p-1)$ are exhibiting $\{100\}$ microfacets.

h	k	l	n	α ($^\circ$)	$\Lambda(\text{Ni})$ (nm)	$\Lambda(\text{Cu})$ (nm)	$\Lambda(\text{Ag})$ (nm)
7	9	9	$8 + 1/3$	6.46	1.810	1.857	2.095
1	3	3	$2 + 1/3$	22.00	0.543	0.557	0.629
2	1	1	$2 + 2/3$	19.47	0.610	0.626	0.707
11	9	9	$9 + 2/3$	5.57	2.096	2.150	2.427

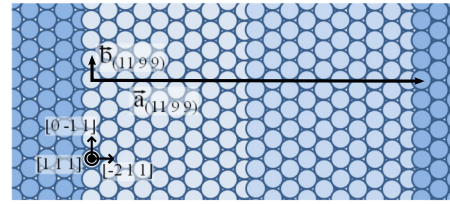


FIG. 2. Schematic drawing of the Ni(11 9 9) surface with the vectors of the (11 9 9) orthogonal basis used as a referential for GIXD measurements. The vector $\vec{c}_{(1199)}$ is perpendicular to the surface.

B. Molecular statics simulations

We have constructed the atomistic models for analyzing the GIXD measurements by means of molecular statics (MS) simulations, using interatomic potentials derived from the second-moment approximation (SMA) of the tight-binding scheme [22]. These potentials have been quite successful in the calculation of bulk [22], surfaces [19,20,23–28], grain boundaries [29,30] and nanoparticles [31,32], equilibrium configurations for both pure metals and binary alloys. The sets of parameters used in the simulations are the same as those used for the study of Ag/Ni(111), which allow us to reproduce respectively the bulk properties for pure metals (cohesive energies, lattice parameters, and elastic properties) and the mixing enthalpies and very low solubility limits for the alloy [27].

The simulation box for these computations consists of two parts:

(i) A rectangular Ni slab with the $[\bar{1}8\ 11\ 11]$, $[0\ \bar{1}\ 1]$, and $[11\ 9\ 9]$ directions parallel to the x , y , and z coordinate axes, respectively. Periodic boundary conditions being applied in the x and y directions, the resulting crystal is then a slab with two (11 9 9) surfaces.

(ii) The Ag layer, which is added row by row starting from a Ni step edge.

The system is fully relaxed using the FIRE (fast inertial relaxation engine) method [33] for each Ag row added on the Ni surface, until temperature falls below 1.10^{-6} K thus ensuring a precision on the total system energy better than 10^{-4} eV. We verify systematically that the slab thickness is sufficient to recover bulk properties in the central layers after relaxation, such as zero pressure and cohesive energy. More precisely, the Ni slab is about $8.4\ \text{nm} \times 1.75\ \text{nm}$ parallel to the surface plane, which corresponds to four (111) terraces in the x direction and seven Ni atoms in the y direction, and 21 nm perpendicular to the surface plane, corresponding to 1000 $[11\ 9\ 9]$ planes in the z direction. In the y direction, we fix the number of Ag atoms to be 6 since it corresponds to the best matching with the Ni lattice parameter, as shown in previous studies [27]. Thus, the system contains at least 28 000 atoms.

III. RESULTS

A. Silver relaxation parallel to the step edges

To understand how the Ag atoms are arranged parallel to the Ni step edges, i.e., along the $[0\ \bar{1}\ 1]$ direction, we have collected a k scan for each sample. Figure 3 presents a characteristic k scan measured at $h_{(1199)} = 0$ and $l_{(1199)} = 0.65$

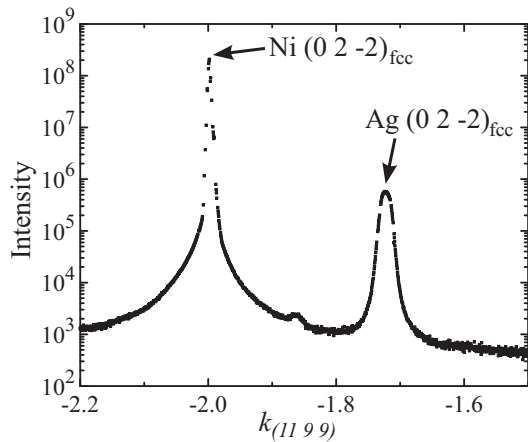


FIG. 3. k scan ($h_{(11\ 9\ 9)} = 0$, $l_{(11\ 9\ 9)} = 0.65$) acquired for 2.5-ML Ag deposition on Ni(11 9 9) annealed at 250 °C.

for a nominal Ag deposition of 2.5 MLs on Ni(11 9 9) followed by an annealing at 250 °C for 1 h. The peak at $k_{(11\ 9\ 9)} = -2.00$ (interplanar distance $d_{\text{exp}} = 0.1246$ nm) corresponds to the $(02\bar{2})_{\text{fcc}}$ Bragg peak of the Ni substrate. The second peak, observed at $k_{(11\ 9\ 9)} = -1.72$ (interplanar distance $d_{\text{exp}} = 0.1446$ nm), is attributed to the $(02\bar{2})_{\text{fcc}}$ Bragg peak of Ag in a fcc structure. From one sample to the other or with the temperature annealing, the measured variation of the Ag peak position is less than 1% (from -1.74 to -1.72), while the Ni one is fixed at the same value ($k_{(11\ 9\ 9)} = -2.00$) for all the samples.

From the two peak positions, we can extract a measured mismatch between Ag and Ni of 0.163 parallel to the step edges. This value has to be compared to the bulk misfit of $\frac{|a_{\text{Ni}} - a_{\text{Ag}}|}{a_{\text{Ni}}} = 0.159$. The good agreement between the measured mismatch and the bulk misfit proves that the Ag layer is relaxed near its bulk parameter parallel to the step edges. This is in agreement with the growth of six Ag atoms on seven Ni atoms (mismatch of 0.167) along the $[0\ \bar{1}\ 1]$ direction as already reported in the literature [27].

B. Thermal evolution of the Ag layer

We have studied the evolution of the Ag layer with the annealing temperature. For a nominal coverage of 3.5 Ag monolayers, Fig. 4 presents h, l maps of the reciprocal space collected at the $k_{(11\ 9\ 9)}$ value corresponding to the Ag peak in order to obtain information about the Ag structure decoupled from the Ni one. The maps are collected at room temperature once the sample is cooled down after each annealing. In the selected range two intense peaks are observed, which can be assigned to Bragg peaks of the Ag fcc structure as indicated in Fig. 4(a). In the as-deposited map [Fig. 4(a)], a large rod along the $[1\ 1\ 1]$ direction is visible. This is the signature of an Ag layer presenting small $(1\ 1\ 1)$ facets. The sample annealing leads to a smoothing of the Ag layer, characterized by a narrowing and finally a disappearance of the $[1\ 1\ 1]$ rod in the h, l maps as the annealing temperature is increased. Concomitantly, the Ag Bragg peaks become thinner, they are more localized, and their intensity increases. Above 250 °C, the $[1\ 1\ 1]$ rod completely disappears to the profit of satellite

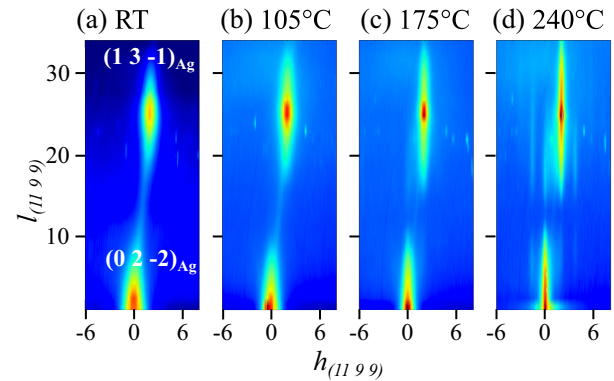


FIG. 4. Evolution of the reciprocal space h, l maps ($k_{(11\ 9\ 9)} = -1.73$) as a function of the annealing temperature for a nominal Ag deposition of 3.5 MLs. The maps are acquired for (a) the as-deposited sample and after annealing at (b) 105 °C, (c) 175 °C and (d) 240 °C. The same color range is used for the four maps. Note that map (a) has been measured at $\mu = 0.3^\circ$ while the others have been acquired at $\mu = 0.15^\circ$, which explains the background modification.

rods parallel to $\vec{c}_{(11\ 9\ 9)}^*$. This means that the $(1\ 1\ 1)$ facets completely disappear while a smooth Ag layer is formed at the interface with the Ni(11 9 9) surface. As will be explained below, two features are observed in the h, l maps after the 250 °C annealing: the satellite rods and the Bragg peaks.

C. Magic heteroepitaxial growth

To go deeper in the analysis of the Ag/Ni interface, we have studied the structure and the orientation of both the Ni substrate and the Ag layer, by collecting larger h, l maps of the reciprocal space at $k_{(11\ 9\ 9)} = -2.00$ and $k_{(11\ 9\ 9)} = -1.72$ for a 2.5-ML Ag deposition on Ni(11 9 9) annealed at 250 °C (see Fig. 5). Both maps present intense peaks and common satellite rods parallel to $c_{(11\ 9\ 9)}^*$. The map measured at $k_{(11\ 9\ 9)} = -2.00$ is related to the Ni substrate, the intense peaks being assigned to the Bragg peaks of the fcc Ni structure. In Fig. 5(a), the indexation of each peak in the fcc basis is reported. The $[1\ 1\ 1]$ direction is clearly identified at an angle of $5.57 \pm 0.05^\circ$ with respect to $\vec{c}_{(11\ 9\ 9)}^*$ confirming the $[11\ 9\ 9]$ orientation of Ni substrate (see Table I).

The map acquired at $k_{(11\ 9\ 9)} = -1.72$ [see Fig. 5(b)] is sensitive to the 2.5-ML-deposited Ag layer. Similarly to the Ni map, the intense peaks can be assigned to the Bragg peaks of the Ag fcc structure. This clearly demonstrates the formation of a perfectly crystallized and oriented Ag layer with its fcc bulk parameter even for a 2.5-ML deposition. The $[1\ 1\ 1]$ direction is at an angle of $6.40 \pm 0.10^\circ$ with respect to $\vec{c}_{(11\ 9\ 9)}^*$, which proves that the Ag layer has a $[7\ 9\ 9]$ orientation as expected for a magic heteroepitaxial growth (see Table I). Moreover, a perfect fcc stacking is observed implying that the layer is homogeneous without any twin formation. Comparing the Ni map and the Ag map, one can observe a symmetry inversion of the Bragg peaks with respect to the $[1\ 1\ 1]$ direction. This indicates that the fcc stacking is reversed from CBA in the Ni substrate to ABC in the Ag layer. The same inversion was also

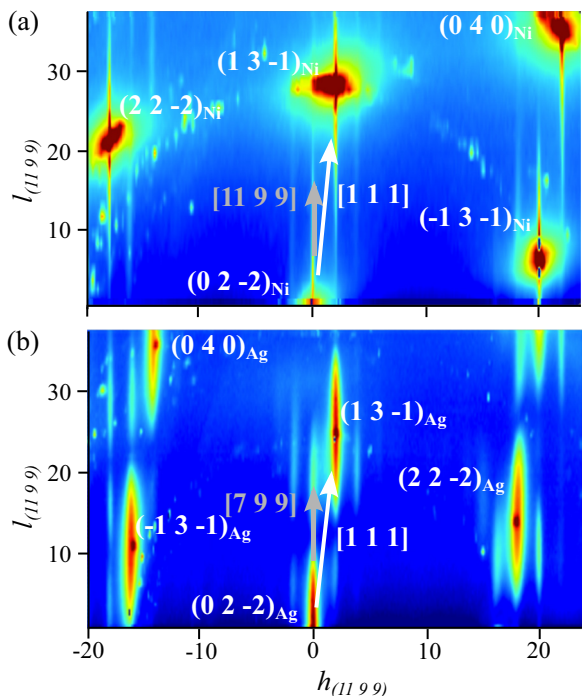


FIG. 5. Reciprocal space h, l maps at (a) $k_{(1199)} = -2.00$ and (b) $k_{(1199)} = -1.72$ for 2.5-ML Ag deposition on Ni(1199) annealed at 250 °C.

observed in the case of Ag growth on Cu(2 1 1) and is coherent with magic heteroepitaxial growth [20,21].

Two features, the satellite rods and the Bragg peaks, are observed in the h, l maps which indicate the presence of two types of diffracting objects on the surface. In both maps, the satellite rods present the same periodicity in h as they are originated from a sharp Ag/Ni interface. The presence of Bragg peaks supposes the formation of well crystallized objects, most probably Ag islands. One can see in Fig. 5(b) that the h positions of the Ag Bragg peaks and the satellite rods do not coincide. Indeed, for example, the $(2\ 2\ \bar{2})_{\text{fcc}}$ Bragg peak is centered at $h_{(1199)} = 18$, which is the expected position for fcc bulk Ag, while the satellite rod is at $h_{(1199)} = 18.13$. This indicates that the Ag islands are well crystallized with the fcc bulk parameter while the interfacial layer is constrained by less than 1%.

D. Stranski-Krastanov growth

To characterize the Ag layer, we have measured precisely some of the Ag rods. Figure 6(a) presents the rod $(18\ -1.72\ l)$, which is passing through the $(22\bar{2})_{\text{fcc}}$ Ag Bragg peak, for two different Ag coverages. The 5-ML sample was obtained by redepositing Ag on the 2.5-ML sample kept at 110 °C. Both rods are characterized by a large base with a superimposed thin peak. One can see that the extra deposition of Ag leads to an increase of the peak height while the base width is preserved. In agreement with h, l maps, this is once again the signature of the presence of well crystallized islands (thin peak) grown on a wetting layer (common base). This is confirmed by STM measurements on the 5-ML-thick sample. Indeed, the STM images reveal the presence on the surface of elongated islands,

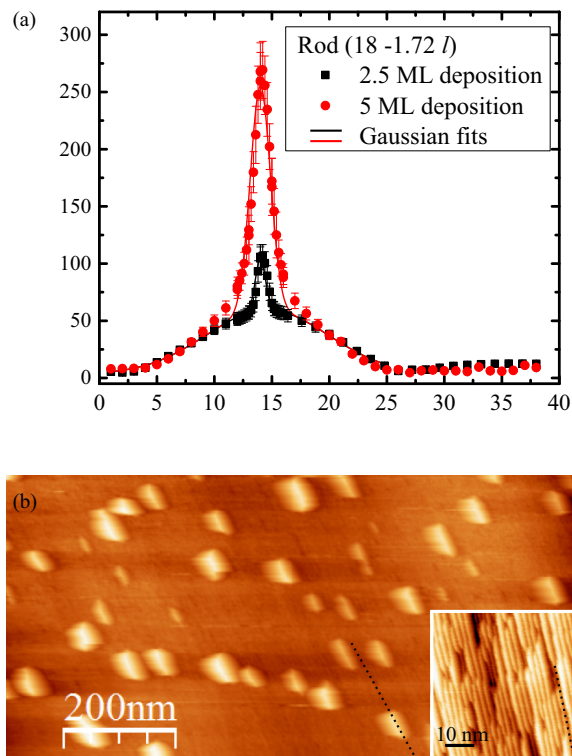


FIG. 6. (a) Rod $(18\ -1.72\ l)$ for two different coverages (2.5 and 5 MLs). (b) STM images of the 5-ML Ag deposition on Ni(1199) at large scale ($V = 2.4\ \text{V}$, $I = 2.5\ \text{nA}$). Inset: STM image in between the islands ($V = 0.9\ \text{V}$, $I = 0.2\ \text{nA}$). In both STM images, the black dotted lines indicate the direction parallel to the Ag step edges.

all having the same orientation [see Fig. 6(b)]. In between the islands, a regular array of terraces is imaged with a period of 2.36 nm [inset of Fig. 6(b)]. In Fig. 6(b), the dotted lines indicate in both STM images the direction of the Ag step edges which corresponds to the island orientation.

To be more quantitative, both the peak and the base are fitted by Gaussian functions [see Fig. 6(a) for the cumulative curves]. For both coverages, the common base presents a full width at half maximum (FWHM) in l of 12.5, which corresponds in real space to a Ag thickness of 0.47 nm. It can be noted that this Ag thickness is slightly larger than twice the Ag monoatomic step height on the $(1\ 1\ 1)$ surface ($2 \times 0.203 = 0.406\ \text{nm}$). For the 2.5-ML deposition the thin peak has a FWHM of 1.02 in l , which corresponds to a height in real space of 6.8 nm. The addition of Ag on the hot sample induced an increase of the FWHM to 2.06 in l , which corresponds to 2.9 nm in real space. This last value can be compared to the apparent heights of the islands measured by STM which are comprised between 1 and 2.5 nm. Despite the large convolution on the island lateral shapes, the measured apparent heights are in agreement with the width of the rod. The extra deposition on the sample leads to the formation of additional small Ag islands which completely dominate the GIXD signal (large peak). The STM images were acquired between the larger islands. Note that a similar behavior has been observed for a 6-ML Ag deposition followed by an annealing at 200 °C for which islands of 6 nm high on a wetting layer were measured by diffraction and STM.

The combination of STM and GIXD measurements enables us to conclude on the formation of well crystallized and oriented Ag islands on a wetting layer. The formation of the Ag wetting layer needs the annealing of the sample. The island size depends on the sample preparation. For deposition on a hot sample (100 °C) small islands are obtained, while postdeposition annealing induces the formation of larger and higher islands.

Finally, Ag grows in the Stranski-Krastanov mode on the Ni(11 9 9) surface, as previously reported for Ni(1 1 1) [10,11]. However, twins are observed in the Ag layer for all previous studies [34,35]. Here, using a well chosen vicinal substrate enables the formation of well crystallized islands on a wetting layer without any stacking fault or twin as expected in the case of a magic epitaxial growth.

E. Ag wetting layer

To be more quantitative about the wetting layer, Fig. 7(a) presents four different rods measured by GIXD (squared data points) and compared to MS simulations (red and blue lines). A scale factor is the only parameter adjusted for the comparison. In Fig. 7(b), the projection of the upper part of the relaxed cell used for the simulation is represented. As explained above, the Ni cell was taken to be thick enough to avoid any motion of

the central atoms. The Ag layer is added row by row along the $[0 \bar{1} 1]$ direction and MS computations are performed at each step. The layer is built starting by adding a first row at the corner of the substrate vicinal surface and completing the first layer by packing nine rows. The second layer is then formed row by row. For each Ag row added, we compared the experimental rods to the simulated ones. It appears that two models reproduce the GIXD data with a good agreement, when the Ag layer is composed of either 17 rows or 18 rows. As can be seen in Fig. 7(b), these two cases correspond to Ag coverage of 2 MLs in our model, as reported in the literature [11]. The main difference between the two models is the position of the Ag step edge with respect to the Ni step edge.

In more detail, for the rods going through Ag-Bragg peaks ($h_{(1199)} = 18, 2, \text{ and } 0$), the rod minimum positions are well reproduced by the 18-row model (red curves in Fig. 7). On the contrary, for the satellite rod ($h_{(1199)} = 4$), the minimum positions are better reproduced by the 17-row model (blue curves in Fig. 7). Most probably, the structure of the wetting layer is intermediate between the two models, possibly with the formation of kinks at the step edges. This last statement is supported by the STM images [see inset in Fig. 6(b)], in which several defects can be observed in the wetting layer. Especially, one can see the presence of secondary steps perpendicular to the Ag step edges (i.e., perpendicular to the dotted line).

IV. SUMMARY

We have studied the growth of Ag on a vicinal Ni(11 9 9) substrate, which is used as a template for the Ag growth. The Ag surface presents an average (7 9 9) orientation and a well defined interface without any intermixing between Ag and Ni, showing that magic heteroepitaxial growth can be extended to vicinal surfaces with large terraces. Moreover, the fcc stacking of the Ag layer is reversed when compared to the Ni substrate fcc stacking and the grown Ag is free from any twin or stacking fault.

However, even though the concept of magic heteroepitaxial growth applies in this case, Ag grows in the Stranski-Krastanov mode, i.e., after the formation of a wetting layer, Ag forms well oriented and crystallized islands. We demonstrate that the wetting layer is limited to 2 MLs and is slightly constrained. The island size then depends on the growth conditions. Deposition at 100 °C induces the formation of small islands while postdeposition annealed at 250 °C enables the ripening towards larger islands. In both cases, the Ag islands are crystallized at the fcc bulk parameter.

It is thus clearly established that the orientation of the Ag layer is governed by the step period. Magic heteroepitaxial growth is equally valid for vicinal surfaces with large terraces and it enables the growth of Ag wetting layer and islands with a unique orientation and without any stacking fault. The combination of vicinal surface and surfactant may lead to the realization of a perfect Ag layer.

ACKNOWLEDGMENT

The authors thank P. Andreazza for the RBS measurements.

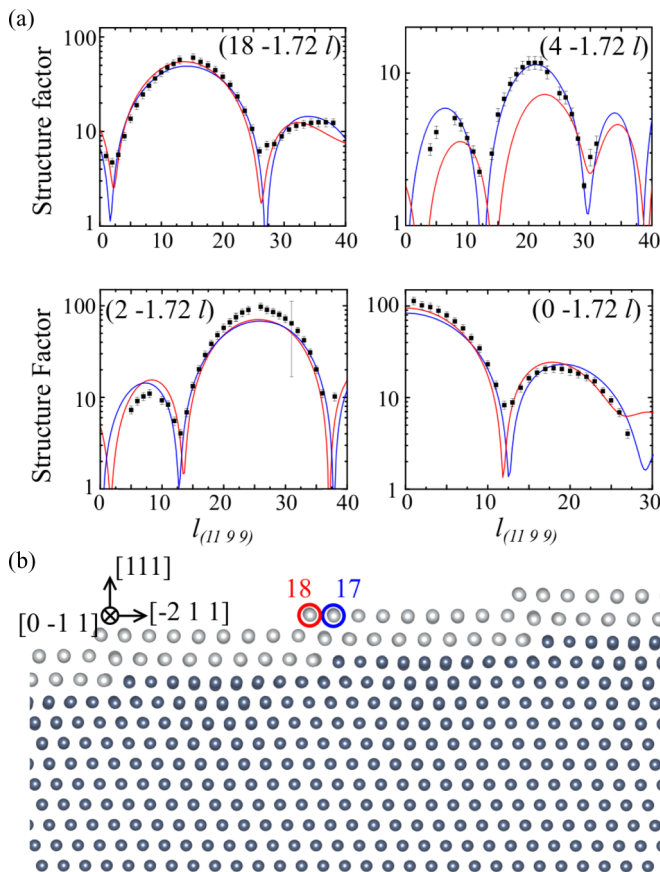


FIG. 7. (a) Rods measured on the Ag(2.5 ML)/Ni(11 9 9) sample compared to the 17-Ag-row (blue curves) and the 18-Ag-row (red curves) models. (b) Schematic of the Ni cell covered by Ag used for the MS calculations.

- [1] J. A. Venables, G. D. T. Spiller, and M. Hanbucken, *Rep. Prog. Phys.* **47**, 399 (1984).
- [2] E. Bauer and J. H. van der Merwe, *Phys. Rev. B* **33**, 3657 (1986).
- [3] Y. Li and A. E. DePristo, *Surf. Sci.* **351**, 189 (1996).
- [4] H. A. Van der Vegt, H. M. Van Pinxteren, M. Lohmeier, E. Vlieg, and J. M. C. Thornton, *Phys. Rev. Lett.* **68**, 3335 (1992).
- [5] M. Li, P.-W. Chung, E. Cox, C. J. Jenks, P. A. Thiel, and J. W. Evans, *Phys. Rev. B* **77**, 033402 (2008).
- [6] H. A. van der Vegt, J. Vrijmoeth, R. J. Behm, and E. Vlieg, *Phys. Rev. B* **57**, 4127 (1998).
- [7] S. A. de Vries, W. J. Huisman, P. Goettkindt, M. J. Zwanenburg, S. L. Bennett, and E. Vlieg, *Phys. Rev. Lett.* **81**, 381 (1998).
- [8] G. W. Jones, J. M. Marcano, J. K. Norskov, and J. A. Venables, *Phys. Rev. Lett.* **65**, 3317 (1990).
- [9] C. Deisl, E. Bertel, M. Bürgener, G. Meister, and A. Goldmann, *Phys. Rev. B* **72**, 155433 (2005).
- [10] V. M. Trontl, P. Pervan, and M. Milun, *Surf. Sci.* **603**, 125 (2009).
- [11] A. Meyer, J. I. Flege, R. E. Rettew, S. D. Senanayake, T. Schmidt, F. M. Alamgir, and J. Falta, *Phys. Rev. B* **82**, 085424 (2010).
- [12] V. Repain, J. M. Berroir, B. Croset, S. Rousset, Y. Garreau, V. H. Etgens, and J. Lecoer, *Phys. Rev. Lett.* **84**, 5367 (2000).
- [13] F. K. Men, F. Liu, P. J. Wang, C. H. Chen, D. L. Cheng, J. L. Lin, and F. J. Himpsel, *Phys. Rev. Lett.* **88**, 096105 (2002).
- [14] A. Bartolini, F. Ercolessi, and E. Tosatti, *Phys. Rev. Lett.* **63**, 872 (1989).
- [15] A. Riemann, B. N. Satterwhite, and B. E. Owens, *Surf. Sci.* **604**, 2157 (2010).
- [16] F.-J. Meyer zur Heringdorf, T. Schmidt, S. Heun, R. Hild, P. Zahl, B. Ressel, E. Bauer, and M. Horn-von Hoegen, *Phys. Rev. Lett.* **86**, 5088 (2001).
- [17] S. Fölsch, A. Helms, S. Zöphel, J. Repp, G. Meyer, and K. H. Rieder, *Phys. Rev. Lett.* **84**, 123 (2000).
- [18] A. R. Bachmann, A. Mugarza, J. E. Ortega, and S. Speller, *Phys. Rev. B* **64**, 153409 (2001).
- [19] A. Coati, J. Creuze, and Y. Garreau, *Phys. Rev. B* **72**, 115424 (2005).
- [20] Y. Garreau, A. Coati, A. Zobelli, and J. Creuze, *Phys. Rev. Lett.* **91**, 116101 (2003).
- [21] Y. Girard, G. Baudot, V. Repain, S. Rohart, S. Rousset, A. Coati, and Y. Garreau, *Phys. Rev. B* **72**, 155434 (2005).
- [22] V. Rosato, M. Guillopé, and B. Legrand, *Philos. Mag. A* **59**, 321 (1989).
- [23] G. Tréglia and B. Legrand, *MRS Proceedings* **491**, 275 (1997).
- [24] R. Tétot, F. Berthier, J. Creuze, I. Meunier, G. Tréglia, and B. Legrand, *Phys. Rev. Lett.* **91**, 176103 (2003).
- [25] I. Braems, F. Berthier, J. Creuze, R. Tétot, and B. Legrand, *Phys. Rev. B* **74**, 113406 (2006).
- [26] I. Braems, J. Creuze, F. Berthier, R. Tétot, and B. Legrand, *Surf. Sci.* **602**, 1903 (2008).
- [27] C. Chambon, J. Creuze, A. Coati, M. Sauvage-Simkin, and Y. Garreau, *Phys. Rev. B* **79**, 125412 (2009).
- [28] C. Chambon, A. Coati, M. Sauvage-Simkin, Y. Garreau, J. Creuze, A. Verdini, A. Cossaro, L. Floreano, and A. Morgante, *Phys. Rev. B* **84**, 165446 (2011).
- [29] J. Creuze, F. Berthier, R. Tétot, and B. Legrand, *Phys. Rev. Lett.* **86**, 5735 (2001).
- [30] J. Creuze, in *Defects and Diffusion in Metals*, Defect and Diffusion Forum Vol. 203–205 (Trans Tech Publications, 2002), pp. 3–36.
- [31] V. Moreno, J. Creuze, F. Berthier, C. Mottet, G. Tréglia, and B. Legrand, *Surf. Sci.* **600**, 5011 (2006).
- [32] L. Delfour, J. Creuze, and B. Legrand, *Phys. Rev. Lett.* **103**, 205701 (2009).
- [33] E. Bitzek, P. Koskinen, F. Gähler, M. Moseler, and P. Gumbsch, *Phys. Rev. Lett.* **97**, 170201 (2006).
- [34] S. Mróz and Z. Jankowski, *Surf. Sci.* **322**, 133 (1995).
- [35] T. Ito, K. Umezawa, and S. Nakanishi, *Appl. Surf. Sci.* **130-132**, 497 (1998).